Damage imaging in plates by evaluating local entropy in guided wavefield data

Erfan Basiri[1], Reza P. R. Hasanzadeh[1]* and Mathias Kersemans[2]
[1]Department of Electrical Engineering, University of Guilan, Rasht, Iran
[2]Mechanics of Materials and Structures, Ghent University, Ghent, Belgium

Abstract— This paper presents a new algorithm called broadband entropy-based two-stage damage imaging (BE2DI) for the detection and imaging of defects in multi-layer plates. The method differentiates defects from either local scattering phenomena of propagating Lamb waves or locally increased vibrational activity for stimulated global plate resonances by exploiting the higher vibrational activity of full-field broadband vibration signals at defective regions and the distinct spatial behavior of defects and artifacts. Using these features, first, a candidate damage map is constructed by means of iterative thresholding based on descriptive statistics of broadband data. After-wards, an adaptive regional damage index based on local entropy is introduced, which utilizes operational deflection shapes to process previously identified candidate regions and subsequently reveal both shallow and deep defects. BE2DI can be seen as an automated local defect resonance identification approach in the case of shallow defects. Multiple plates having various defect types with different sizes and depths are investigated. Broadband chirp signals are used to excite the plates using low-power piezoelectric actuators, and vibrational data is registered by 3D scanning laser Doppler vibrometry. The obtained results quantitatively and qualitatively demonstrate that the proposed method can effectively detect different kinds of damage, regardless of being shallow or deep.

Keywords: **Multi-layer plates, Non-destructive testing, Operational deflection shape, Local entropy, Guided waves, Laser Doppler vibrometry**

Abbreviations: Nondestructive testing (NDT), Scanning laser Doppler vibrometer (SLDV), Local defect resonance (LDR), Operational deflection shape (ODS), Carbon fiber reinforced polymers (CFRP), Piezoelectric transducer (PZT), Defect-to-background ratio (DBR), Root mean square (RMS), True positive (TP), False positive (FP), Preliminary candidate damage map (PCDM), Candidate damage map (CDM), Adaptive regional damage index (AR-DI), Adaptive damage index (A-DI), Broadband entropy-based two-stage damage imaging (BE2DI)

* Corresponding author: hasanzadehpak@guilan.ac.ir

1. INTRODUCTION

Having high stiffness and strength along with low weight, composite materials are being used in a wide variety of applications, including the automotive and aerospace industries. Nevertheless, composites are prone to the formation of internal damage, most of which occurs during the production process or operational lifetime. Hence, nondestructive testing (NDT) methods are critical to monitoring the composite parts of structures

Amongst the different fields of NDT, vibrometric NDT has proven to be promising to detect various types of defects in large composites. In such methods, the specimen is excited using high-frequency acoustic waves (≥100 kHz), generated by either piezoelectric contact transducers [1], air-coupled transducers [2], or non-contact (scanning) pulsed lasers [3,4]. Using a pulse laser for excitation, a vibrometric NDT method can become completely non-contact; however, the downside is that it might not sufficiently excite higher modes of guided waves [4]. Afterwards, the guided waves are registered, which can be either based on contact or a non-contact transducer. Non-contact registration of guided waves could be achieved by means of a scanning laser Doppler vibrometer (SLDV) or air-coupled transducers [5,6]. The main advantage of SLDV over traditional methods is providing the possibility of automatic measurement over a large number of grid points with an arbitrary resolution. However, sensing vibrations using SLDV is often time-consuming due to the fact that several measurements are essential to improve the signal- to-noise ratio. For a reduction of inspection time, one can either alter the setup and use a continuous or multi-beam SLDV [7,8], or reduce the measurement points using wavefield reconstruction methods, including compressed sensing techniques [9–11]. Alternatively, sparse guided wave inspection is another approach wherein data is obtained from a predefined sensor network to reconstruct damage maps through various signal processing algorithms. In this regard, [12] considered signal matching compression by sparse reconstruction method combined with sum and delay imaging approach for detecting damage, while [13,14] employed temporal entropy to identify sudden energy changes in the recorded guided wave signals and link it to damage features.

In recent years, several methods have been proposed to detect defects using full-field vibrational data from different perspectives: energy- based methods [15], wavenumber filtering [16–20], learning methods [21,22],

wavelet-based [23,24], curvature analysis [25], and local defect resonance [26–40], amongst others. Between the methods, the local defect resonance (LDR) technique has gained great attention. LDR phenomenon was first observed in [26] and then further developed by Solodov and other research groups in the recent decade [27,28]. When a guided wave meets a defect, efficient energy trapping can occur if its frequency coincides with the natural frequency of the defect. On the premise that the residual thickness is sufficient at the defect, considerable energy is continually applied to the defect for some time by the trapped wave, which can lead to the formation of a standing wave and resonance at specific frequencies. This resonance is named LDR. What makes LDR-based techniques advantageous amongst other guided wave detection methodologies is their capability to work at lower frequencies, detect defects in the vicinity of the edge and locate defects regardless of being in small or large plates. Moreover, there is no need to scan a plate with dense scan point spacing, resulting in lower measurement time.

LDR can cause a further increase in the local vibrational activity at a defect, enhancing the preexisting increase due to the local stiffness reduction of the defect. Hence, one can achieve good visual contrast between the defective and sound area by finding the LDR frequency of the defect and then observing the operational deflection shape (ODS) at that frequency. Moreover, the application of LDR is not confined to certain types of defects and can be used for both linear and nonlinear defects. How the LDR frequency should be found without any previous knowledge regarding the location of the defect and then how it should be used to detect either linear or nonlinear defects have been the main questions over the past few years, and various methodologies have attempted to answer them from different perspectives [29–40].

There exist forms of defect that exhibit nonlinear characteristic; that is, they vibrate in more than one harmonic. It is possible to distinguish such defects from the sound area by accurate detection of higher harmonics from the lower ones which accounts for the vibration of the healthy area. In the case that the excitation frequency matches the LDR frequency of a defect, by taking advantage of the more efficient nonlinear components generated by the LDR, this scheme can lead to even higher contrast. Based on the previously explained methodology, multiple nonlinear signal processing strategies have been proposed to detect

LDR frequency. Authors in [31–33] employed frequency spectrum analysis to detect LDR frequencies. In another method, bicoherence analysis is performed instead of the discrete Fourier transform, which allows the LDR frequency to be automatically derived for non- linear defects [34]. In [35], using the scaling subtraction method, nonlinear components of the vibration signal are separated from the linear ones, and then LDR frequency is determined via identifying the highest peak of the resulting signal. In the same research, the authors also demonstrated that using LDR frequency as the probing frequency leads to better damage map rather than selecting any other frequencies. Authors in [36] used short time Fourier transform to extract higher harmonics and subsequent band power calculation to pinpoint deep and shallow delaminations. Since LDR contains higher harmonics, band power improves defect detectability.

All previously described damage detection methods work by taking advantage of the nonlinearity imposed by defects. However, this nonlinearity can only be triggered by a sufficiently high excitation power. In [37], an automated approach is introduced for the detection of shallow and relatively deep defects merely via the linear effects of LDR frequency. The process involves data compression followed by an iterative amplitude thresholding to detect LDR frequency for various defects, including flat bottom holes (FBHs), inserts (artificial de-laminations), and barely visible impact damage (BVID). A subcategory of LDR-based methods includes those based on the fusion of ODSs, aiming to mitigating possible artifacts of elastic waves. Artifacts spatially occur at distinct locations in various ODSs, whereas for defects, it is in opposite [41]. [40] investigated this concept in lattice sandwich structures, where the full-field narrowband response of the plate is obtained with periodic tone burst excitation, and then inner product is used to fuse ODSs to localize defects. Albeit providing an acceptable result, the manually selection of excitation signal frequency band tuned to the resonance frequencies of the defects and its inability to function with broadband excitation are the limitations of the method. More recently, [39] proposed a method for automatic extraction of local defect resonance in woven CFRPs using laser-generated guided waves, where wavenumber filtering combined with a wave attenuation compensation technique is used to preemptively eliminate the disturbances resulting from the weave structure in advance of LDR frequency identification for damage map construction. Linear LDR-based defect detection

methods are successful in detecting shallow defects. However, they cannot be used to pinpoint deep defects [38]. In fact, [38] demonstrated that in the case of a deep defect, the resonance frequency converges to the global resonance frequency of a plate and therefore no LDR occurs in such defects.

Energy-based methods are another line of research in vibrometric for defect detection, where the increase in the local vibrational activity of defects is exploited for defect localization. The most basic signal processing approach is root mean square (RMS) [15], which computes the energy of out-of-plane vibration per scan point to construct a damage map. Albeit revealing shallow defects, this method is not sufficiently sensitive to deep defects owing to the imperceptible difference between the vibrational activity of deep defects and the surrounding sound area. Authors in [38] introduced a weighted band power calculation using a directional dependent wave attenuation factor, which is more sensitive to both shallow and deep defects compared to the RMS approach.

As elaborated above, achieving high-contrast damage maps sensitive to defects with various sizes and depths is still a challenge for vibro-metric LDR and energy-based signal processing methods. To address this issue, this study proposes a novel NDT damage detection methodology, called broadband entropy-based two-stage damage imaging (BE2DI) wherein the physical advantages of both energy and LDR-based methods are used. In the first stage, a candidate damage map is generated through the descriptive statistics of broadband vibrational response data. Within this map, different regions are observed, which can be linked to the presence of a defect, elastic wave scattering artifacts, or locally increased vibrational activity caused by global resonation of the plate. In the second stage, the generated candidate damage map is analyzed by an adaptive regional damage index to differentiate true positive (TP) from false positive (FP) candidate regions, followed by the construction of the final damage map by employing the concept of spatial local entropy. The high performance of the proposed BE2DI methodology is demonstrated on several (sandwich) composite plates with various defects types, sizes, and depths.

The structure of the paper can be summarized as follows: section 2 describes the experimental setup. The physical background and the two stages of BE2DI are elaborated in sections 3 and 4, respectively. Section 5

discusses the damage detection capability of BE2DI for several plates with various defects. Finally, the paper is concluded in section 6.

2. MATERIALS AND EXPERIMENTS

Experiments are performed on two carbon fiber reinforced polymers (CFRPs), one aluminum alloy, and one sandwich plate with dissimilar defects. The first sample, $CFRP_1$, is a compression-molded CFRP laminate sized $330 \times 330 \times 5.52$ mm³ with a layup $[(+45/0/-45/90)_3]_s$. Eleven flat bottom holes (FBHs) of varying remaining thicknesses and diameters are created on the backside of the plate. The second sample, $CFRP_2$, is a CFRP laminate sized $330 \times 330 \times 3$ mm³ with a layup $[(0/90)_3]_s$, manufactured using resin transfer molding and containing twelve inserts of different depths and sizes. The third sample, AL, is an $400 \times 400 \times 5$ mm³ aluminum plate containing 10 FBHs with the same diameter but different remaining thicknesses. The last sample, CFRP-AR, is a $250 \times 225 \times 7$ mm³ sandwich panel symmetric in the thickness direction. It is comprised of following layers: a 1 mm thick pre-cured woven CFRP plate with layup [22 twill /+ − 45 biax / 22 twill], a 163 g/m^2 epoxy adhesive film, a Nomex aramid honeycomb core with cell size 4.8 mm and thickness 5 mm, an additional layer of epoxy adhesive film, and another pre-cured woven CFRP. Prior to stacking the layers, a small area of BVID in the frontside CFRP plate is introduced by hammer hitting, and a 30×30 mm^3 cutout in the first layer of epoxy adhesive film. The cutout resulted in a disbond between the core and the skin plate after oven-curing. BVID and disbond represent realistic types of damage occurring in real-world scenarios. The backside of all mono-lithic composite laminates and the inspection side of CFRP-AR are shown in Fig. 1. Moreover, the specifications of the defects contained in the first three plates, including relative thickness u, radius of FBHs, and size of inserts, are incorporated in the figure. We consider a defect with $u < 50\%$ as a shallow defect; otherwise, it is considered a deep defect.

A chirp signal is applied to the specimens through surface-bonded piezoelectric transducers (PZTs) to excite broadband elastic waves. The PZT is bonded to the backside of the plates, and the excitation frequency ranges from 5 kHz to 150 kHz for $CFRP_1$ and from 1 kHz to 100 kHz for $CFRP_2$, AL, and CFRP-AR. The excitation

signal is amplified to 50 Vpp for the monolithic laminates and 150 Vpp for the Nomex using a Falco System WMA-300 voltage amplifier. A 3D infrared SLDV (Polytec PSV-500 3D Xtra) is used to measure the vibration velocity at the front surface of the plates. For each scan point, the three vibration velocity components are measured in a predefined uniform grid spacing. In this work, only the out-of-plane vibration component is analyzed. Fig. 2 provides a schematic representation of the experimental methodology and lists several experimental settings. In the figure, $U_{exc}(x, y, t)$ and $V_z(x, y, t)$ respectively represent the excitation signal and the measured out-of-plane velocity.

Fig. 1 Here

Fig. 2 Here

3. PHYSICAL BACKGROUND

Axiom I (intensified local vibrational activity): To explain this axiom, defect-to-background ratio (DBR) is defined as (1) and is dis-played for FBH_9 (shallow defect) and FBH_{11} (deep defect) within $CFRP_1$ in Fig. 3(a, b) respectively [38]:

$$DBR(f) = \frac{n_h}{n_d} \frac{\sum_{i=1}^{n_d} V_z(x_i, y_i, f)}{\sum_{i=1}^{n_h} V_z(x_i, y_i, f)}. \quad (1)$$

n_d and n_h are the number of measurement points within the defected area being investigated and surrounding healthy area, respectively. $V_z(x_i, y_i, f)$ is the magnitude of the out-of-plane velocity of a point with coordinates (x_i, y_i) at frequency f. Local flexural stiffness reduction at defects causes defective points to have higher vibrational activity compared to the sound area. This is observed in Fig. 3(a, b) where, for substantial frequencies, the DBR exceeds 1 for both shallow and deep FBHs. Due to the large flexural stiffness reduction at FBH9, this higher vibrational activity clearly manifests itself as LDR in the ODS corresponding to the largest peak of the DBR curve in Fig. 3, denoted as f_1. In the case of FBH_{11}, flexural stiffness reduction is too small to develop such LDR phenomenon (see the ODS related to f_2 in Fig. 3) [38]. Nevertheless, it is still possible to observe the effect of stiffness reduction as slightly intensified local vibrational activity in specific ODSs (for example, see the ODS corresponding to f_3 in the figure). Although the localized pattern within the circle is

replicated throughout the entire plate, indicating its association with global plate resonance, the local vibration at FBH_{11} is more pronounced compared to other regions of the composite.

Axiom II (distinct spatial behavior between artifacts and defects): Elastic wave artifacts can be categorized as follows: scattered waves converted to other modes or reflected from plate boundaries and signal distortions caused by temperature changes and surface variations [40–42]. The mentioned artifacts spatially occur at distinct locations in various ODSs due to the different wave speeds of modes and distinct frequencies. In the context of deep defect detection, the global resonances of the plate can be perceived as an artifact due to their analogous spatial behavior with the vibrational activity of deep defects [40]. Similarly, this phenomenon spatially occurs at different locations of a plate at different frequencies. Contrary to artifacts and global resonances of the plate, the local vibration of a defect is present in the same position across different ODSs.

Fig. 3 Here

4. BROADBAND ENTROPY-BASED TWO-STAGE DAMAGE IMAGING (BE2DI)

The intensified vibrational activity at defects, together with the distinct spatial behavior between defects and artifacts, results in ODSs containing exclusive defect-related information, each providing unique information about the extent of a defect. This offers an opportunity for detecting both shallow and deep defects via the proper fusion of selected ODSs.

The proposed BE2DI methodology comprises two main stages. To benefit from axiom I, some defective candidate points are required to be identified in advance. Section 4.1 is responsible for generating such a candidate map. In section 4.2, inspired by the algorithm proposed in [40] and exploiting the combination of axioms I and II, the previously obtained damage candidates are investigated and processed through an adaptive regional damage index to obtain a single damage map for the plate being studied. The proposed damage methodology is detailed on the experimental dataset obtained for sample $CFRP_1$ and the flowchart provided in Fig. 4 displays different signal and data processing steps of BE2DI.

Fig. 4 Here

4.1 CANDIDATE GENERATION

Exploiting the higher vibrational activity of defective regions, a preliminary candidate damage map (PCDM) can be obtained with a simple thresholding per scan point (x, y) as follows:

$$PCDM(x,y) = \underset{f}{num}\ \{V_z(x,y,f) > \delta_{PCDM}\}. \quad (2)$$

The operator num computes the number of frequencies whose amplitude is higher than a certain threshold level denoted as δ_{PCDM}. Fig. 5 illustrates $PCDM$ for different values of δ_{PCDM}. Knowledge on the location of shallow defects can be easily achieved using various thresholds values. For scan points corresponding to deep defects, however, the computed $PCDM$ value is often very similar to the $PCDM$ value of scan points from the healthy region. Despite this, lower thresholds still show higher vibrational activity for deep defects compared to the rest of the plate. Therefore, a $PCDM$ with a well-chosen value for δ_{PCDM}, where defects exhibit increased intensity while healthy area have low amplitude, serves as a promising starting point to generate a candidate damage map.

In the following of this section, first, a reasonable strategy is introduced to automatically determine δ_{PCDM} through analyzing peaks of broadband data with Renyi entropy. Then, via an iterative thresholding method based on the descriptive statistics of $PCDM$ a candidate damage map is obtained. The top part of Fig. 4 shows the process of candidate map generation discussed in 4.1.

Fig. 5 Here

4.1.1 AUTOMATIC δ_{PCDM} COMPUTATION

Generally speaking, as shown in Fig. 6(a), the area surrounding the PZT (indicated in red) has larger peaks compared to both defective areas (indicated in purple) and the remaining part (indicated in black) of the coupon. Conversely, the defective area shows more vibrational activity and larger peaks compared to the healthy area. Consequently, a threshold between the strong peaks of the defective area and the area surrounding PZT could be a suitable choice for δ_{PCDM}. Then, a fundamental question arises: which peak of the signals should be utilized? To address this, let us analyze Fig. 6(b). In the figure, each damage map, denoted as $IP(x, y, j)$, represents the j

-th largest peak at every scan point's velocity spectrum, where $j = 1,5,10,\dots,J$. For brevity, only the results related to j equals 1, 40 and 50 are illustrated. Comparing the obtained images to each other, it can be observed that the contrast be-tween the defects and the sound area is more noticeable in some of them. Hence, a threshold based on the peak corresponding to the sharpest IP, denoted as β-th peak, can be a good choice for δ_{PCDM}. From Fig. 6(a), it can be seen that a sufficient difference exists between the peaks of defects and the sound area when a threshold is set between the lowest and highest β-th peak of all signals (see the highlighted peaks with orange arrows and the green dashed line between them in Fig. 6(a)). To obtain β automatically, Renyi entropy [43] can be used as demonstrating the contrast of an image:

$$\beta = \underset{j=1}{\overset{J}{argmax}} \left(-\sum_{x=1}^{M} \sum_{y=1}^{N} log\ |IP(x,y,j)|^3\right) \quad (3)$$

In (3), considering that smaller peaks are likely to be more affected by noise and thus might not have meaningful information, a sensible value of J can be determined as follows: first, the scan point with the middle value in the $IP(x,y,1)$ is chosen, and its location is named $(\tilde{x},\tilde{y})$. Then, the number of peaks corresponding to $V_z(\tilde{x},\tilde{y},f)$ whose amplitude is bigger than half of the amplitude of the biggest peak in the signal is determined, and J is set to it.

Finally, to ensure that δ_{PCDM} falls between the lowest and highest β-th peak of signals, δ_{PCDM} is set as follows:

$$\delta_{PCDM} = \mu_{IP(x,y,\beta)} + \xi_1\, \sigma_{IP(x,y,\beta)}. \quad (4)$$

Here, $\mu_{IP\,(x,y,\beta)}$ and $\sigma_{IP(x,y,\beta)}$ denote the global mean and standard deviation of the $IP(x,y,\beta)$, respectively. This is done because the majority of the plate consists of sound area scan points, causing the mean converges towards the vibrations of non-defected area. Since the threshold selection process aims to ensure that the required amount of vibrational activity characteristic to defective regions satisfies δ_{PCDM} while dropping a considerable amount of vibrational activity related to sound areas, $\sigma_{IP(x,y,\beta)}$ is added to the mean. This way, in the presence of defects in the plate, the difference between the magnitudes of the defective and healthy peaks increases the threshold, leading to the subsequent cancellation of sound area vibration. The constant parameter

ξ_1 determines the degree to which the standard deviation affects the threshold. Empirical experiments have shown that the appropriate value of ξ_1 typically falls between 1 and 2. For the purposes of this study, we chose the value of 1.5 for the remainder of the paper. The resulting $PCDM$ is presented in the first part of Fig. 4.

Fig. 6 Here

4.1.2 CANDIDATE DAMAGE MAP (CDM)

Areas with a high likelihood of being damaged in $PCDM$ are selected as candidates using an iterative thresholding method. Candidates are points with intensities greater than the average $PCDM$ plus three times the standard deviation. The average and standard deviation are computed subsequent to excluding previous candidates in the preceding iteration. The thresholding is iterative because all generated candidates initially belong to either high elevated region around the PZT or shallow defects displaying high vibrational activity, preventing the points corresponding to lower vibrational activity, potentially associated with less severe defects, from being revealed. If no point exceeds the threshold, the threshold is reduced by 5 percent in the next iteration. This process proceeds until 50% of the plate is chosen as candidates, assuming that damage does not cover more than half of the inspected area.

As defects appear in form of a region rather than a single point, it is advised to work with candidate regions instead of candidate scan points. Fig. 4 displays CDM constructed from some selected candidate regions (R), each constructed of a set of scan points denoted as $\{(x_1, y_1), (x_2, y_2), \cdots, (x_{n_p}, y_{n_p})\}$ with n_p indicating the number of points. In the iteration process, if a candidate region overlaps with one from the previous iteration, both regions are considered candidates, and each is separately processed in the second stage of BE2DI. It should be noted that some scan points with high intensity due to the elevated power around the PZT can be initially removed through the $PCDM$'s biggest region containing the location of the bonded PZT.

4.2 DAMAGE IMAGING

The second stage of BE2DI introduces an adaptive regional damage index (AR-DI), to process candidate regions in CDM and subsequently reveals a defect through the proper fusion of selected ODSs. Moreover, it

is shown that the proposed damage index can simultaneously distinguish FP regions from TP ones as a result of axiom II. The second part of Fig. 4 provides an overview of the proposed damage imaging method-ology, which is further detailed in Algorithm I.

Algorithm I

4.2.1 ODS SELECTION BASED ON LOCAL ENTROPY

The process begins by selecting a point (x_R, y_R) from region R in CDM. Before fusing the ODSs, it is essential to arrange them in descending order based on the local contrast of ODSs in the vicinity of the point (x_R, y_R). This is crucial because the higher the local contrast within a particular ODS, the more it contributes to the detection of damage (see axiom I). This behavior can be quantified by computing the local entropy. Accordingly, using the first two steps of Algorithm I, the ODSs are sorted, and their respective frequencies are listed in $\tilde{f}$.

4.2.2 ADAPTIVE REGIONAL DAMAGE INDEX (AR-DI)

Next, an adaptive damage index (A–DI) based on local inner product is employed to fuse the square of previously sorted ODSs (energy of ODSs) to generate a single image [40]:

$$A\text{-}DI\ (x, y, x_R, y_{R,}\alpha) = \sum_{a=1}^{m} \sum_{b=1}^{m} \prod_{i=1}^{\alpha} V_z(x + a, y + b, \tilde{f}(i))^2 \quad (5)$$

where $A\text{-}DI\ (x, y, x_R, y_{R,}\alpha)$ is the resulting image value at point (x, y) constructed from ODSs sorted based on local entropy around (x_R, y_R); m is the kernel size and is set to 3, and the free parameter α indicates the number of ODSs selected from the vector $\tilde{f}$. Amongst different fusion method, inner product is preferred because it combines geometric mean and gamma transform. Geometric mean helps to reduce the intensity of artifacts and global resonances while keeping the intensity of the central portion of the region being investigated by finding the central tendency of values. Gamma transform then narrows the range of bright values, increasing the contrast between the background and the under- investigation region R [44].

Afterwards, considering that $A-DI$ corresponding to different points within R has their unique information, section 4.2.1 and (5) are repeated for every point within R. The results are then scaled by their mean and summed as follows:

$$AR\text{-}DI\ (x,y,R,\alpha) = \sum_{i=1}^{n_p} \frac{A\text{-}DI\ (x,y,x_i,y_i,\alpha)}{\underset{(x,y)}{mean}\ A\text{-}DI\ (x,y,x_i,y_i\alpha)}. \quad (6)$$

The resulting map $AR\text{-}DI$ stands for regional $A\text{-}DI$, and $AR\text{-}DI\ (x,y,R,\alpha)$ is the resulting image value at the point (x,y). (6) is favored over averaging, as giving more weight to $A\text{-}DI$ maps with high contrast at R results in a higher-quality map [17]. The effectiveness of $AR\text{-}DI$ greatly relies on the value of α, determining the number of ODSs being included in the computation. In the next two subsections, the effect of α is investigated, and then an automatic approach is proposed for its computation. Afterwards, the first two stage previously discussed in 4.2.1 and 4.2.2 are separately repeated for all candidate regions to obtain the corresponding AR-DI map.

4.2.3 Exploring the impact of α on $AR\text{-}DI$ construction

As an example, Fig. 7 illustrates $AR\text{-}DI$ construction as a function of α for three candidate regions previously denoted in the CDM map in Fig. 4, namely R^{FBH_9}, $R^{FBH_{11}}$, and R^{FP_1}. An automated masking algorithm, based on the maximum value of candidate regions in $PCDM$, is applied through Algorithm II to prevent the regions with higher vibrational activity from obscuring the region R being studied. Additionally, the excitation location and its surrounding elevated region are automatically cropped out (in the case that it is unknown) using the $PCDM$'s biggest region containing the location of the bonded PZT.

Concerning TP regions, the increase of α leads to a more uniform background thanks to (5) by mitigating the high-intensity zones originating from global resonances or other artifacts and incorporating heightened vibrational activity of the defects in different frequencies (see axiom II). This effect arises because the mentioned non-ideal terms are not present in the same location across ODSs and are thus mitigated by the inner product. On the other hand, the central part of defects re-mains unaffected in earlier ODSs, which is due to the consistent vibrational activity within the damaged area across them. Inclusion of later ODSs underestimates the

magnitude of defects since defect borders do not demonstrate significant activity throughout all ODSs. This under-estimation leads to the convergence of under-investigated zones to the inner product kernel size (see Fig. 7).

The same behavior as that of TP representing deep FBH is observed for the FP region, but with more high-intensity zones coexisting in more $AR-DI$ maps. This results from the simultaneous appearance of multiple high-intensity zones throughout selected ODSs with the FP region due to the impact of the global resonance of the plate. This, in turn, is caused by the inclusion of more ODSs in (6) until only one zone related to the FP region remains. Similar to TP regions, the corresponding high-intensity zone is left in the map with increasing α, resulting from the ODSs previously being sorted based on local entropy. It should be noted that one can even predict the extent of damage, as the deeper a defect is, the larger the optimal α becomes.

Fig. 7 Here

Algorithm II

4.2.4 Optimal α and TP vs. FP region discrimination

As observed, the behavior of TP and FP regions differs in $AR-DI$ maps, which can serve a dual purpose: the automatic computation of the optimal α and the differentiation of TP from FP regions. Since it is not known whether the region being processed is TP or FP, the objective is to opt α in a way that maximizes the contrast for the region being processed in the entire AR-DI. In this regard, first, following contrast function C [37] is computed for different α values ranging from 1 to the number of frequency frames N of the SLDV data:

$$C(\alpha)=\frac{\underset{(x,y)\in R}{mean}\ \text{AR-DI}\ (x,y,R,\alpha)}{\underset{(x,y)\notin R}{mean}\ \text{AR-DI}\ (x,y,R,\alpha)} \tag{7}$$

Since $AR-DI$ is constructed based on sorted ODSs, an increase in the obtained curve with the increase of α is expected. If a decrease occurs in C, it indicates either that the size of R is considerably underestimated or low quality ODSs (wherein the vibration activity is strong at healthy area due to the global resonances of the plate) in terms of uniformity are included in the computation of $AR-DI$. Accordingly, the $AR-DI$ corresponding to the first peak of the C curve, denoted as α_{ini}, can be a good initial point for decision. To compute the number of

regions in $AR\text{-}DI\ (x, y, \alpha_{ini}, R)$, Otsu thresholding [45] is applied, and the resulting binary images are processed. If the resulting binary map has more than one region, it is considered a FP region because even at α_{ini}, the binary map has multiple regions. If there is one isolated region, R is considered TP, and then the smallest α leading to an $AR\text{-}DI$ whose binary map has only one region is chosen as the optimal α. Using the proposed algorithm, the optimal α is determined as 1 for the shallow FBH_9, indicating that BE2DI operates as an automated LDR identification algorithm. For the TP corresponding to the deep defect, a value of α = 5 is obtained, while the value of α corresponds to 12 for the selected FP region. The results can visually be verified using the actual size of the defect indicated with a green dashed line in Fig. 7. It should be noted that in the case of two $AR - DI$ maps corresponding to two TP candidate regions that overlap with each other and both belong to a certain defect, the one resulting in a single zone while having best match with its corresponding candidate region in size is chosen. This section is abridged in the step 3 to 9 of Algorithm I.

5. RESULTS AND COMPARATIVE STUDY

Here, the application of BE2DI on various plates introduced in section 2 is demonstrated and discussed. For the space limitation, $AR\text{-}DI$ maps corresponding to qualified candidate regions are aggregated as follows: the values of highlighted zones in each map are directly transferred to the final damage map, and for the remaining material, pixels are assigned the average of all $AR\text{-}DI$ maps. The BE2DI computation takes around 15 minutes with an Intel Core (TM) i7-8700K CPU @ 3.70 GHz and 16 GB RAM memory for each specimen. It is possible to reduce the time through parallel processing, as the computation of $AR\text{-}DI$ per candidate region is independent of each other.

Moreover, for the purpose of comparison and a better understanding of how BE2DI functions, it is compared with RMS [15], the primary benchmark method in guided wavefield defect detection algorithm. It is worth noting again that, as shown in section 3 and detailed in the comprehensive parametric finite element study in [38], there is no existence of LDR behavior in shallow defects, and thus, it can be said that the proposed BE2DI outperforms LDR identification methods in terms of defect detectability. As such, it is avoided to compare BE2DI with such methods in the following subsections.

5.1. $CFRP_1$

Upon the implementation of the previously mentioned methods, the resulting damage maps are presented in Fig. 8. Constructed by aggregating the $AR\text{-}DI$ maps corresponding to the TP regions, the results indicates that BE2DI yields better damage detection performance compared to the RMS. Whilst RMS could not well detect the deep defects and deal with the elevated region surrounding PZT, the proposed method proves highly sensitive to all defects and can reveal them with high contrast. The result confirms that the second stage of BE2DI could decently mitigate artifacts and differentiate between the FP and TP candidates provided by its first stage (see associated CDM map in Fig. 4).

Fig. 8 Here

5.2. $CFRP_2$

The results for $CFRP_2$, which contains square inserts to mimic delamination defects, are presented in Fig. 9. In the result of the RMS, it can be readily verified that the inserts did not result in nice square-shaped delamination defects. It seems that the inserts are at some areas somewhat attached to the CFRP material, leading to complex-shaped delamination defects. Further, $CFRP_2$ has a cross-ply stacking sequence leading to distinct wave propagation along the horizontal and vertical directions. This can be easily seen in the corresponding RMS map, presenting a challenge for processing algorithms to pinpoint defects I_6 and I_{11}. Visually speaking, most defects are somewhat localized by both damage detection algorithms, complying with the fact that $u \leq 50$ % for all inserts, and thus defects have sufficient energy compared to their sound area to be detected. The elevated region comprising a large portion of CFRP, however, is a significant drawback for RMS, making it incapable of detecting I_6 and I_{11}. Visually speaking, BE2DI is successful in detecting various-sized inserts, including the two challenging ones. This implies that the introduced algorithm has the potential to be utilized in the case of anisotropic composites knowing that none of its steps depend on the direction of propagation waves. Moreover, the contrast between the defective regions and their corresponding sound area is significantly improved compared to RMS, which can be validated through contrast-to-noise (CNR) computation as follows:

$$CNR = 20\ log\ \left|\frac{M_{defect} - M_{sound}}{\sigma_{sound}}\right| \quad (8)$$

where M_{defect} and M_{sound} are respectively the mean of the scan points in the defective and sound area, and σ_{sound} denotes the standard deviation of the sound area. The sound area is considered the circular region surrounding the defective region with a radius twice the size of the defect. The CNR values listed in Table 1 are in agreement with abovementioned claim.

One might observe the inconsistency between the size of the identified defects and their actual size. In the case of smaller inserts in size, this inconsistency arises because that LDR does not occur in the whole region of a shallow insert. Regarding deep inserts, wherein the optimal α is bigger than 1, in addition to the aforementioned reason, the dual nature of the inner product (see Section 4.2.3) affects the sizing. If exact sizing is of interest, the algorithm may be extended by giving more weight to the outer parts of the studied region when computing the inner product. This is, however, not considered in the current study as the focus is put on high-contrast defect imaging.

Fig. 9 and Table 1 Here

5.3. AL

BE2DI is applied to the AL and displayed in Fig. 10 to verify that its application is not limited to CFRP. In the constructed maps in Fig. 10, the vibrational activity in the region around the PZT is less pronounced due to the lower material damping of the Al plate when compared to the CFRP plates. Fig. 10 illustrates the enhanced damage detectability of BE2DI compared to RMS in the case of defects with $u \geq 50\ \%$, especially FBH_9 which is regarded as a very deep defect. The higher contrast of BE2DI compared to the RMS in the case of two shallow and deep defects is shown in the figure. The only defect that is not detected is FBH_{10} with relative depth of $u = 93\ \%$. For such an extremely deep defect, the generated vibrational activity is not sufficient to be captured by the first stage of BE2DI. However, it is possible to obtain sufficient energy by removing A0 related to the sound area vibration using mode filtering approaches [4,17] and then applying BE2DI to the broadband vibrational data.

Fig. 10 Here

5.4. CFRP-AR

At last, both BE2DI and RMS are applied to the vibrational data obtained for CFRP-AR, and the respective results are shown in Fig. 11. The RMS map shows poor performance in detecting and highlighting both defects, instead the RMS map is dominated by the strong radiation of the excitation PZT. The proposed BE2DI method on the other hand results in a high-contrast map in which both BVID and the disbond are highlighted.

Fig. 11 Here

6. CONCLUSION

In this study, a method called BE2DI is proposed to address the defect detection problem in plates using full-field vibrational surface data. The high performance of the method is demonstrated on CFRP, Al-alloy, and sandwich plates with different defect types (FBHs, inserts, disbond, and BVID), depths, and sizes. The proposed damage imaging method comprises two stages. In the first stage, a candidate map is generated by an iterative thresholding method based on descriptive statistics of SLDV data. The second stage offers an automated damage index using hitherto identified candidate regions to generate a final damage map, exploiting locally intensified pattern in some well-chosen ODSs through an algorithm based on local entropy. The obtained damage maps demonstrate the capability of BE2DI to detect both shallow and deep defects with high contrast in different types of composites, highlighting its superiority over RMS and LDR-identification methods in detecting profound structural defects.

Notwithstanding the fact that BE2DI provide a high-contrast damage map, it is not designed for the accurate sizing of defects, and it comes with a certain computational cost. Future work might focus on the extension of BE2DI for accurate sizing of different damage types with lower computational cost. In addition, it might be instructive to statistically investigate the performance of BE2DI for a large set of experiments and to determine probability of damage detection curves.

REFERENCES

[1] W. Ostachowicz, M. Radzieński, and P. Kudela, "50th Anniversary Article: Comparison Studies of Full

Wavefield Signal Processing for Crack Detection," Strain, vol. 50, no. 4, pp. 275-291, Jun. 2014.

[2] M. Jurek, M. Radzienski, P. Kudela, and W. Ostachowicz, "Non-contact excitation and focusing of guided waves in CFRP composite plate by air-coupled transducers for application in damage detection," Procedia Structural Integrity, vol. 13, pp. 2089-2094, 2018.

[3] E. B. Flynn, S. Y. Chong, G. J. Jarmer, and J.-R. Lee, "Structural imaging through local wavenumber estimation of guided waves," NDT & E International, vol. 59, pp. 1-10, Oct. 2013.

[4] J. Segers, S. Hedayatrasa, G. Poelman, W. Van Paepegem, and M. Kersemans, "Self-reference broadband local wavenumber estimation (SRB-LWE) for defect assessment in composites," Mechanical Systems and Signal Processing, vol. 163, p. 108142, Jan. 2022.

[5] M. Castaings and P. Cawley, "The generation, propagation, and detection of Lamb waves in plates using air-coupled ultrasonic transducers," The Journal of the Acoustical Society of America, vol. 100, no. 5, pp. 3070-3077, Nov. 1996.

[6] C. T. Truong, D.-H. Kang, J.-R. Lee, and C. R. Farrar, "Comparative Study of Laser Doppler Vibrometer and Capacitive Air-coupled Transducer for Ultrasonic Propagation Imager and the New Development of an Efficient Ultrasonic Wavenumber Imaging Algorithm," Strain, vol. 51, no. 4, pp. 332-342, Jun. 2015.

[7] K. Yuan and W. D. Zhu, “A novel general-purpose three-dimensional continuously scanning laser Doppler vibrometer system for full-field vibration measurement of a structure with a curved surface,” Journal of Sound and Vibration, vol. 540, p. 117274, Dec. 2022.

[8] Y. Li, J. Zhu, M. Duperron, P. O’Brien, R. Schüler, S. Aasmul, M. de Melis, M. Kersemans, and R. Baets, “Six-beam homodyne laser Doppler vibrometry based on silicon photonics technology,” Optics Express, vol. 26, no. 3, p. 3638, Feb. 2018.

[9] A. Ijjeh, S. Ullah, M. Radzienski, and P. Kudela, "Deep learning super-resolution for the reconstruction of full wavefield of Lamb waves," Mechanical Systems and Signal Processing, vol. 186, p. 109878, Mar. 2023.

[10] S. Sabeti and J. B. Harley, "Spatio-temporal undersampling: Recovering ultrasonic guided wavefields from incomplete data with compressive sensing," Mechanical Systems and Signal Processing, vol. 140, p. 106694,

Jun. 2020.

[11] Y. Keshmiri Esfandabadi, L. De Marchi, N. Testoni, A. Marzani, and G. Masetti, "Full Wavefield Analysis and Damage Imaging Through Compressive Sensing in Lamb Wave Inspections," IEEE Transactions on Ultrasonics, Ferroelectrics, and Frequency Control, vol. 65, no. 2, pp. 269-280, Feb. 2018.

[12] C. Xu, Z. Yang, S. Tian, and X. Chen, “Lamb wave inspection for composite laminates using a combined method of sparse reconstruction and delay-and-sum,” Composite Structures, vol. 223, p. 110973, Sep. 2019.

[13] A. Baltazar, E. Rojas, and R. Mijarez, “Structural Health Monitoring in Cylindrical Structures Using Helical Guided Wave Propagation,” Physics Procedia, vol. 70, pp. 686–689, 2015.

[14] E. Rojas, A. Baltazar, and K. J. Loh, “Damage detection using the signal entropy of an ultrasonic sensor network,” Smart Materials and Structures, vol. 24, no. 7, p. 075008, Jun. 2015.

[15] A. Żak, M. Radzieński, M. Krawczuk, and W. Ostachowicz, "Damage detection strategies based on propagation of guided elastic waves," Smart Materials and Structures, vol. 21, no. 3, p. 035024, Feb. 2012.

[16] P. Kudela, M. Radzieński, and W. Ostachowicz, “Identification of cracks in thin-walled structures by means of wavenumber filtering,” Mechanical Systems and Signal Processing, vol. 50–51, pp. 456–466, Jan. 2015.

[17] J. Segers, S. Hedayatrasa, G. Poelman, W. Van Paepegem, and M. Kersemans, “Robust and baseline-free full-field defect detection in complex composite parts through weighted broadband energy mapping of mode-removed guided waves,” Mechanical Systems and Signal Processing, vol. 151, p. 107360, Apr. 2021.

[18] M. Barzegar, D. J. Pasadas, A. L. Ribeiro, H. G. Ramos, Y. Lugovtsova, and J. Bulling, “Polar Coordinate for Damage Imaging of Adhesively Bonded Plates Using Ultrasonic Guided Waves and Laser Doppler Vibrometer Measurements,” IEEE Transactions on Instrumentation and Measurement, vol. 72, pp. 1–11, 2023.

[19] F. Gao, Y. Shao, J. Hua, L. Zeng, and J. Lin, “Enhanced wavefield imaging method for impact damage detection in composite laminates via laser-generated Lamb waves,” Measurement, vol. 173, p. 108639, Mar. 2021.

[20] T. Kang, M. Yoon, S. Han, K.-M. Kim, and B. Koo, “Selection of optimal exciting frequency and Lamb

wave mode for detecting wall-thinning in plates using scanning laser Doppler vibrometer," Measurement, vol. 200, p. 111676, Aug. 2022.

[21] A. A. Ijjeh and P. Kudela, "Deep learning-based segmentation using full wavefield processing for delamination identification: A comparative study," Mechanical Systems and Signal Processing, vol. 168, p. 108671, Apr. 2022.

[22] S. Ullah, A. A. Ijjeh, and P. Kudela, "Deep learning approach for delamination identification using animation of Lamb waves," Engineering Applications of Artificial Intelligence, vol. 117, p. 105520, Jan. 2023.

[23] G. Sha, M. Radzienski, R. Soman, T. Wandowski, M. Cao, and W. Ostachowicz, "Delamination imaging in laminated composite plates using 2D wavelet analysis of guided wavefields," Smart Materials and Structures, vol. 30, no. 1, p. 015001, Nov. 2020.

[24] W. Zhou, Y. F. Xu, and J. S. Kim, "Baseline-free structural damage identification for plate-like structures based on two-dimensional curvature propagating flexural waves," Journal of Sound and Vibration, vol. 536, p. 117098, Oct. 2022.

[25] G. Sha, H. Xu, M. Radzieński, M. Cao, W. Ostachowicz, and Z. Su, "Guided wavefield curvature imaging of invisible damage in composite structures," Mechanical Systems and Signal Processing, vol. 150, p. 107240, Mar. 2021.

[26] L. H. Tenek, E. G. Henneke, and M. D. Gunzburger, "Vibration of delaminated composite plates and some applications to non-destructive testing," Composite Structures, vol. 23, no. 3, pp. 253-262, Jan. 1993.

[27] I. Solodov, J. Bai, S. Bekgulyan, and G. Busse, "A local defect resonance to enhance acoustic wave-defect interaction in ultrasonic nondestructive evaluation," Applied Physics Letters, vol. 99, no. 21, p. 211911, Nov. 2011.

[28] I. Solodov and M. Kreutzbruck, "Local defect resonance of a through-thickness crack," Ultrasonics, vol. 118, p. 106565, Jan. 2022.

[29] J. Segers, S. Hedayatrasa, G. Poelman, W. Van Paepegem, and M. Kersemans, "Backside delamination detection in composites through local defect resonance induced nonlinear source behavior," Journal of Sound

and Vibration, vol. 479, p. 115360, Aug. 2020.

[30] S. Hadi, R. P. R. Hasanzadeh and M. Kersemans, "A Defect Image Enhancement Approach for Detection of Defective Area in CFRPs Through Local Defect Resonance," 2020 International Conference on Machine Vision and Image Processing (MVIP), 2020.

[31] D. Ginzburg, F. Ciampa, G. Scarselli, and M. Meo, "SHM of single lap adhesive joints using subharmonic frequencies," Smart Materials and Structures, vol. 26, no. 10, p. 105018, Sep. 2017.

[32] G. P. Malfense Fierro and M. Meo, "Nonlinear elastic imaging of barely visible impact damage in composite structures using a constructive nonlinear array sweep technique," Ultrasonics, vol. 90, pp. 125-143, Nov. 2018.

[33] G. P. M. Fierro, D. Ginzburg, F. Ciampa, and M. Meo, “Imaging of Barely Visible Impact Damage on a Complex Composite Stiffened Panel Using a Nonlinear Ultrasound Stimulated Thermography Approach,” Journal of Nondestructive Evaluation, vol. 36, no. 4, Sep. 2017.

[34] S. Roy, T. Bose, and K. Debnath, "Detection of local defect resonance frequencies using bicoherence analysis," Journal of Sound and Vibration, vol. 443, pp. 703-716, Mar. 2019.

[35] L. Wei and J. Chen, "Determination of optimal probing frequency for enhancing nonlinear vibro-acoustic modulation behaviors of delaminated CFRP based on local defect resonance, " Mechanical Systems and Signal Processing, vol. 187, p. 109961, Mar. 2023.

[36] J. Segers, S. Hedayatrasa, G. Poelman, W. Van Paepegem, and M. Kersemans, "Nonlinear Elastic Wave Energy Imaging for the Detection and Localization of In-Sight and Out-of-Sight Defects in Composites," Applied Sciences, vol. 10, no. 11, p. 3924, Jun. 2020.

[37] J. Segers, S. Hedayatrasa, E. Verboven, G. Poelman, W. Van Paepegem, and M. Kersemans, "Efficient automated extraction of local defect resonance parameters in fiber reinforced polymers using data compression and iterative amplitude thresholding," Journal of Sound and Vibration, vol. 463, p. 114958, Dec. 2019.

[38] J. Segers, S. Hedayatrasa, G. Poelman, W. Van Paepegem, and M. Kersemans, "Probing the limits of full-field linear local defect resonance identification for deep defect detection," Ultrasonics, vol. 105, p. 106130, Jul.

2020.

[39] Z. Lan, O. Saito, F. Yu, and Y. Okabe, “Impact damage detection in woven CFRP laminates based on a local defect resonance technique with laser ultrasonics,” Mechanical Systems and Signal Processing, vol. 207, p. 110929, Jan. 2024.

[40] K. Feng, Q. Zhao, and Z. Li, "Baseline-Free Damage Identification Method for Lattice Sandwich Structures Based on Operational Deflection Shapes," Research in Nondestructive Evaluation, vol. 32, no. 3-4, pp. 147-159, Jul. 2021.

[41] J. E. Michaels and T. E. Michaels, “Guided wave signal processing and image fusion for in situ damage localization in plates,” Wave Motion, vol. 44, no. 6, pp. 482–492, Jun. 2007.

[42] K. Yang, S. Kim, and J. B. Harley, “Unsupervised long-term damage detection in an uncontrolled environment through optimal autoencoder,” Mechanical Systems and Signal Processing, vol. 199, p. 110473, Sep. 2023.

[43] Z. K. Peng, G. Meng, F. L. Chu, Z. Q. Lang, W. M. Zhang, and Y. Yang, "Polynomial Chirplet Transform with Application to Instantaneous Frequency Estimation," IEEE Transactions on Instrumentation and Measurement, vol. 60, no. 9, pp. 3222-3229, Sep. 2011.

[44] R. C. Gonzalez and R. E. Woods, Digital Image Processing, 3rd ed. Hoboken, NJ, USA: Pearson, 2008.

[45] N. Otsu, “A Threshold Selection Method from Gray-Level Histograms,” IEEE Transactions on Systems, Man, and Cybernetics, vol. 9, no. 1, pp. 62–66, Jan. 1979.

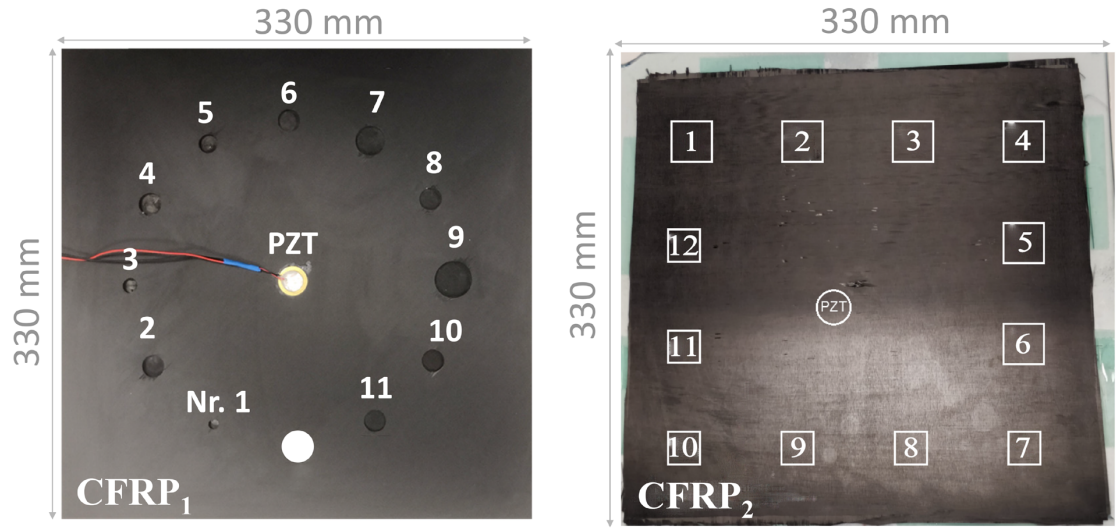

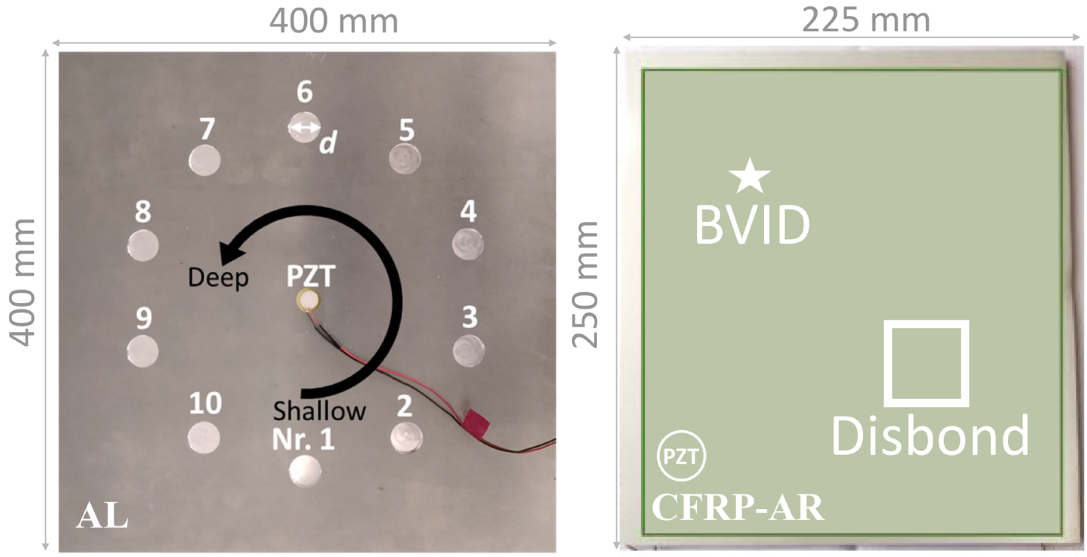

CFRP1	Defect name	FBH1	FBH2	FBH3	FBH4	FBH5	FBH6	FBH7	FBH8	FBH9	FBH10	FBH11
	d (mm)	7	15	10	15	12.5	15	20	15	25	15	15
	u (%)	29	20	31	29	30	39	31	49	31	58	67

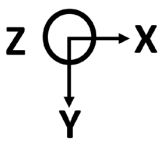

CFRP2	Defect name	I1	I2	I3	I4	I5	I6	I7	I8	I9	I10	I11	I12
	s (mm)	20					15						
	u (%)	8	16	25	33	42	50	8	16	25	33	42	50

AL	Defect name	FBH1	FBH2	FBH3	FBH4	FBH5	FBH6	FBH7	FBH8	FBH9	FBH10
	d (mm)	35									
	u (%)	9	13	20	30	43	57	64	71	83	93

Fig. 1. Inspected coupons along with the specification of the defects are presented.

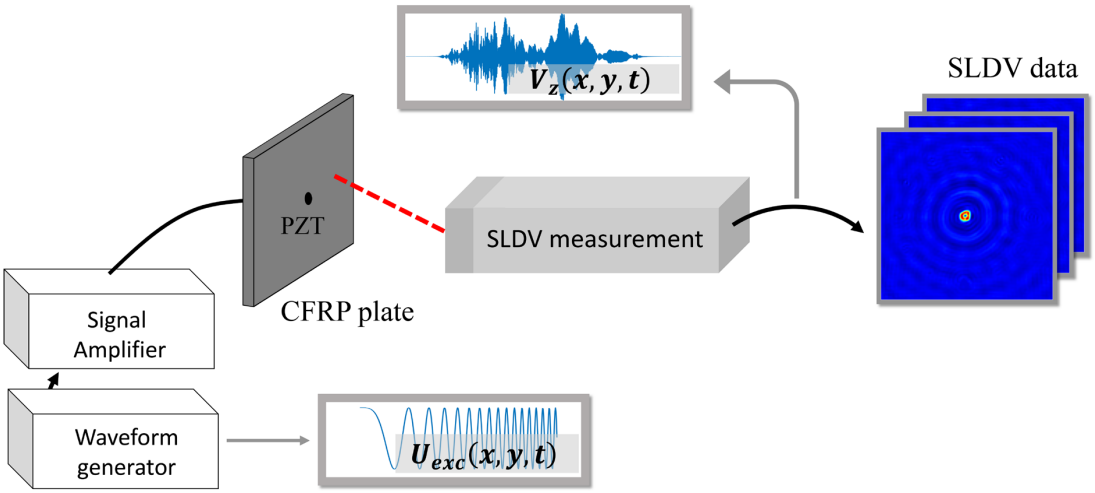

Plate	Excitation		SLDV			
	F_{beg} (kHz)	F_{end} (kHz)	# Scan points	# Time samples	Grid size (mm)	Fs (MHz)
$CFRP_1$	5	150	14640	10000	2.5	1.25
$CFRP_2$	1	100	20449	10000	2.5	0.625
AL	1	100	14883	10000	2.5	0.25
CFRP−AR	2	100	12402	10000	2.5	0.625

Fig. 2. Schematic illustration of the data acquisition systems with the detailed experiments specifications.

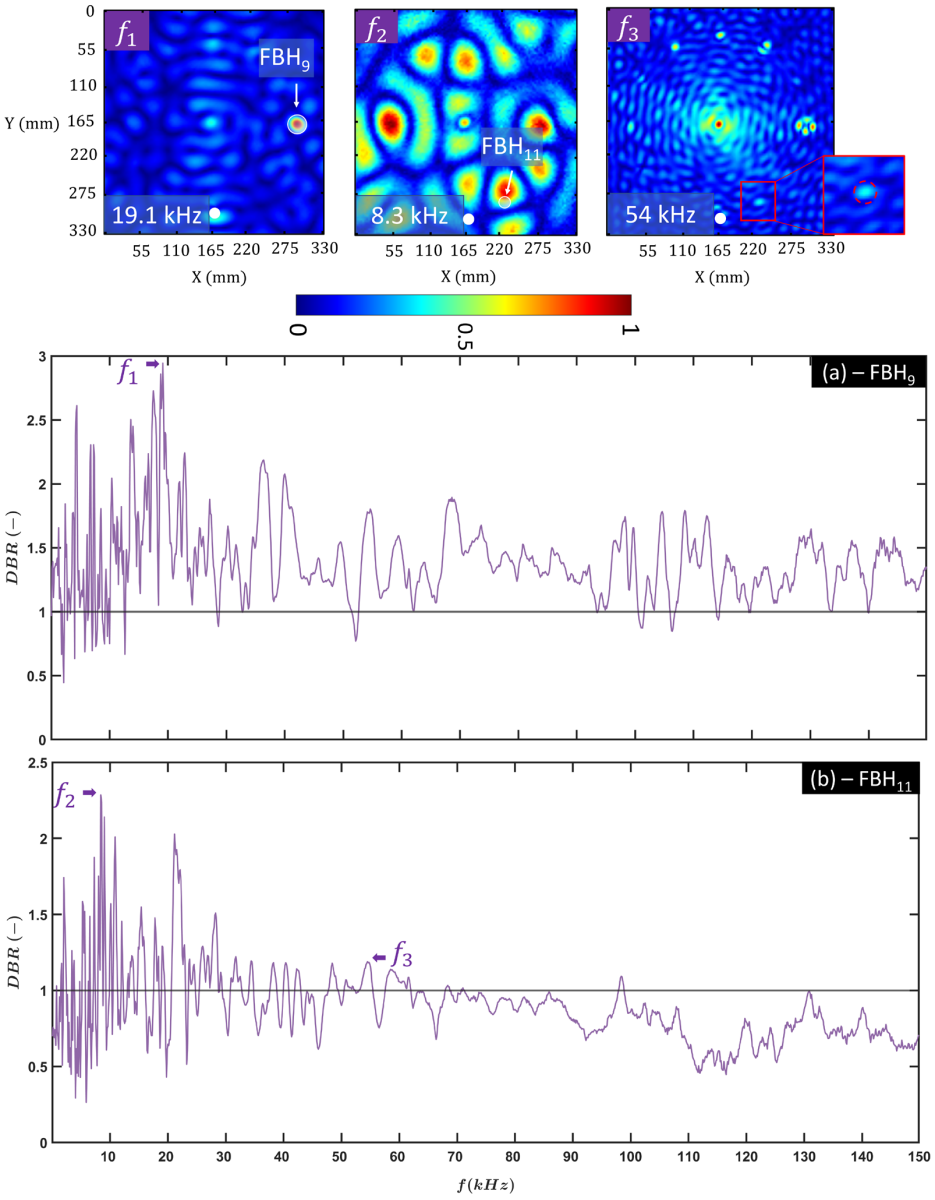

Fig. 3. (a, b) DBR curves for FBH_9 and FBH_{11}, respectively. Several ODSs corresponding to the frequencies of the largest peaks of FBH_9 and FBH_{11}, denoted as f_1 and f_2, and a frequency at which FBH_{11} exhibits discernible local vibrational activity, denoted as f_3, are displayed.

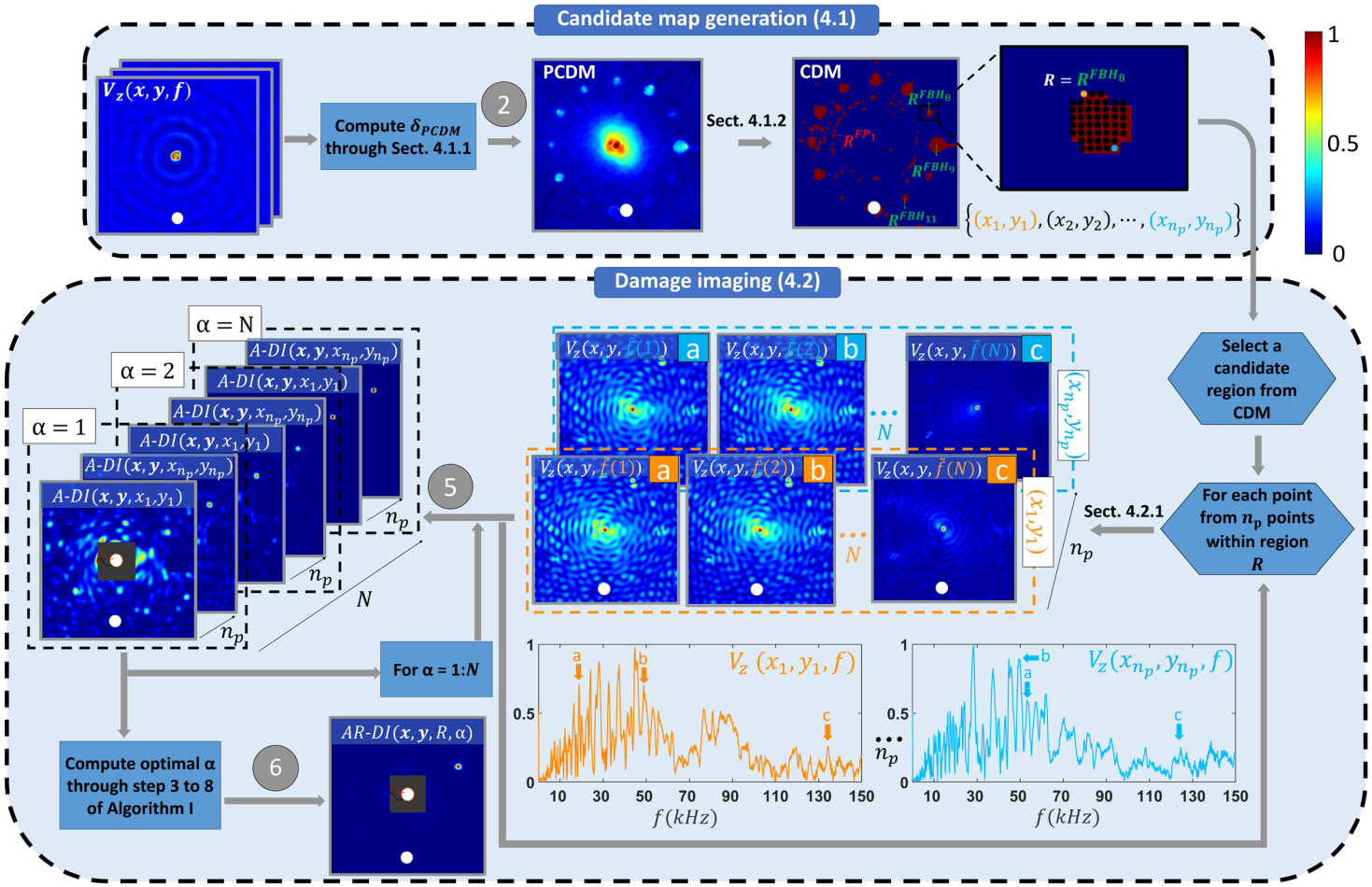

Fig. 4. A schematic overview of the BE2DI algorithm. As an example, a FP and three TP regions are depicted in the CDM. TP regions denoted as R^{FBH_8}, R^{FBH_9} and $R^{FBH_{11}}$ respectively represent FBH8, FBH$_9$ and FBH$_{11}$. R^{FP_1} corresponds to a FP region. Moreover, the second stage of the method is indicated for two exemplary scan points (x_1, y_1) and (x_{n_p}, y_{n_p}) from R^{FBH_8} (see the zoomed image).

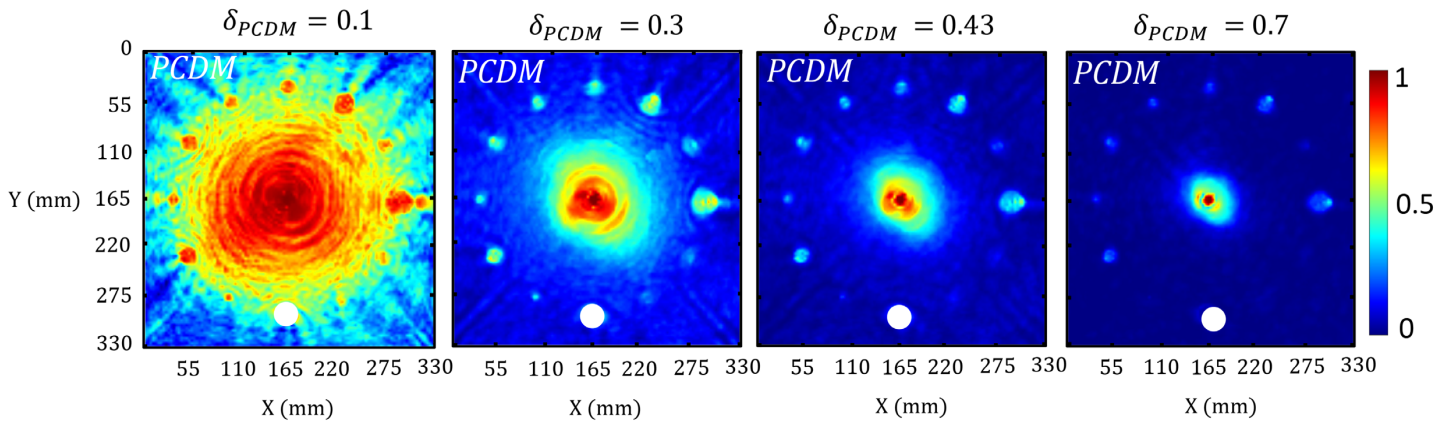

Fig. 5. $PCDM$ calculated as a function of δ_{PCDM}

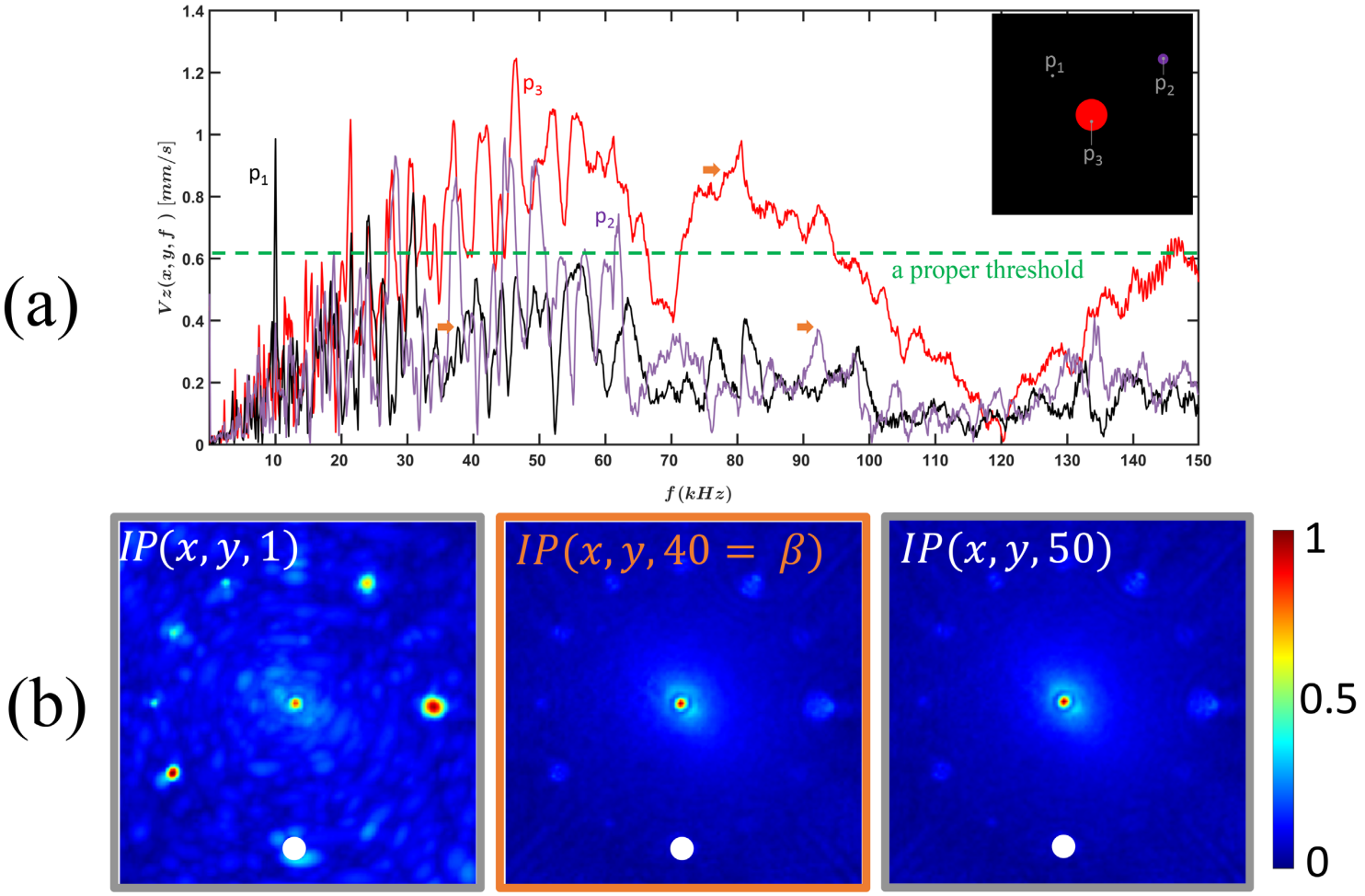

Fig. 6 (a) The velocities corresponding to three points, P_1, P_2, and P_3, are respectively plotted in **black**, **purple**, and **red** to illustrate the principle of automatically determining δ_{PCDM}. As an example, a proper δ_{PCDM} is shown in **green**. (b) $IP(x,y,j)$ as a function of j. $IP(x,y,40=\beta)$ is selected as the sharpest image using (3). The β-th peaks of the aforementioned three points are marked with **orange** arrows in (a).

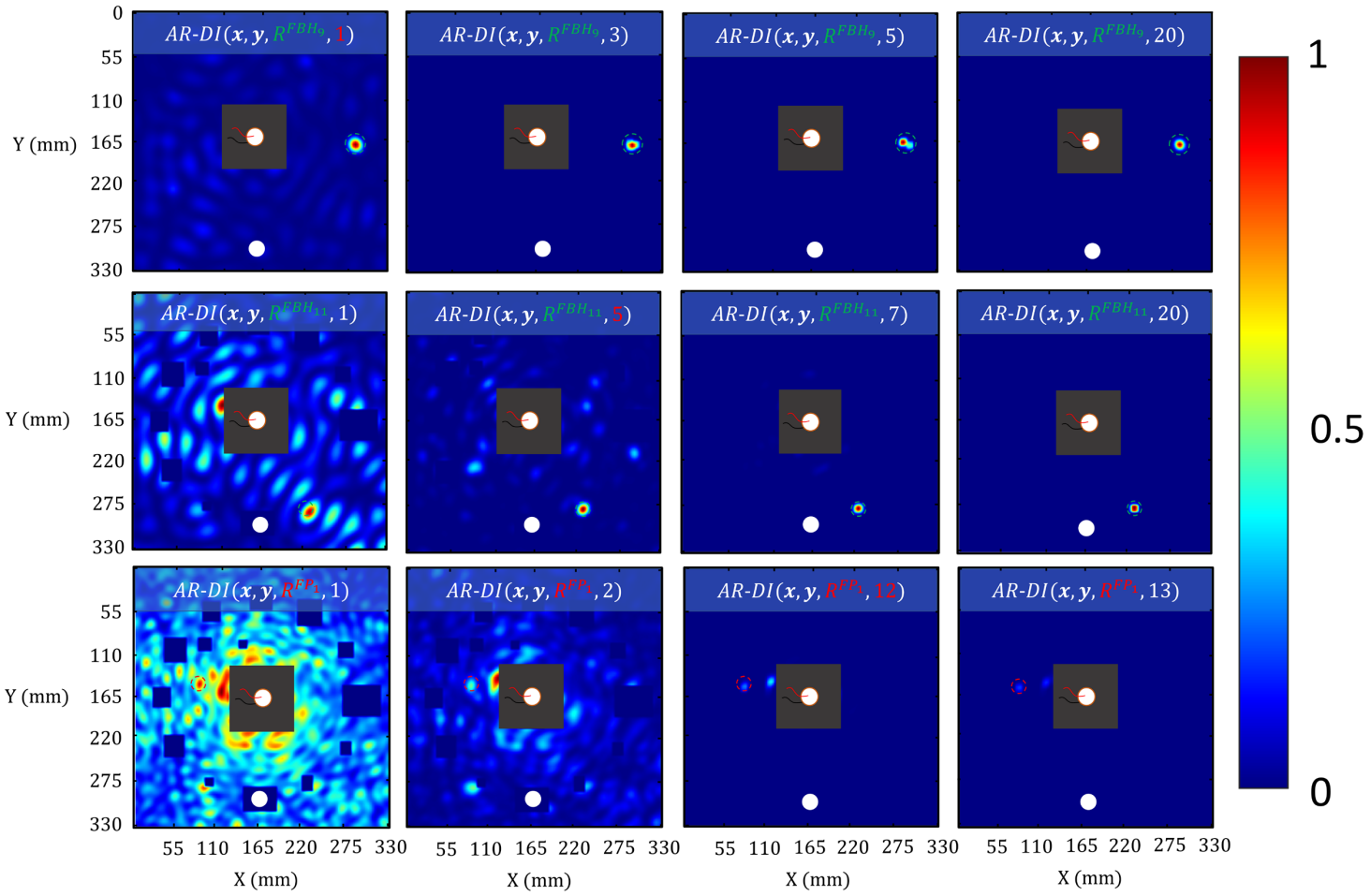

Fig. 7. From top to bottom, each row respectively shows maps calculated as a function of α for two TP candidate, R^{FBH_9} and $R^{FBH_{11}}$, and one FP region R^{FP_1} previously depicted in the CDM map in Fig. 4. The actual size of TP regions, in conjunction with the location of the candidate regions for the FP region, is respectively indicated with green and red dashed circles on the maps. The optimal value of α for different regions is written in red.

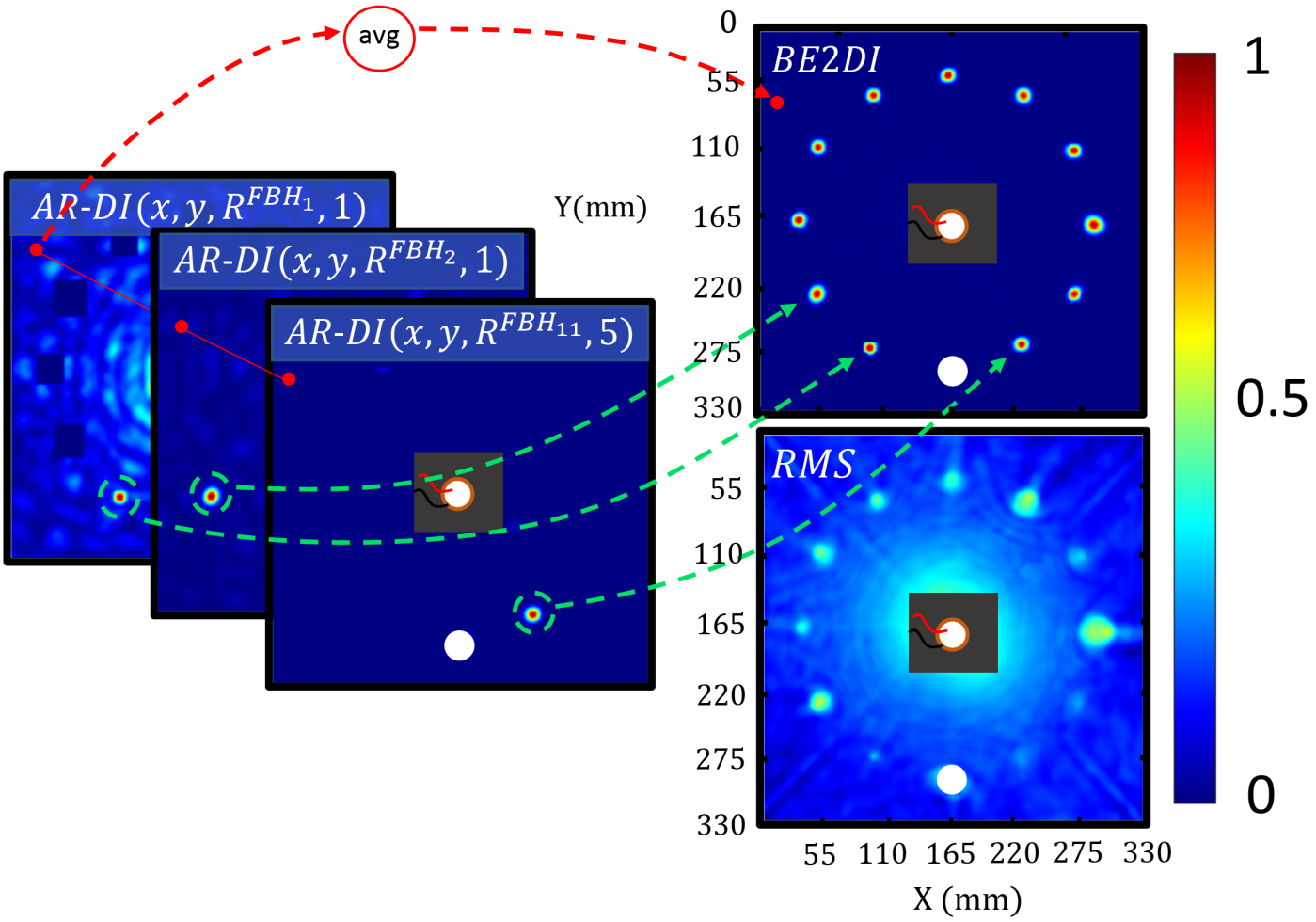

Fig. 8. Normalized results of RMS and BE2DI on $CFRP_1$, along with an illustration demonstrating how *AR-DI* maps are aggregated, are provided.

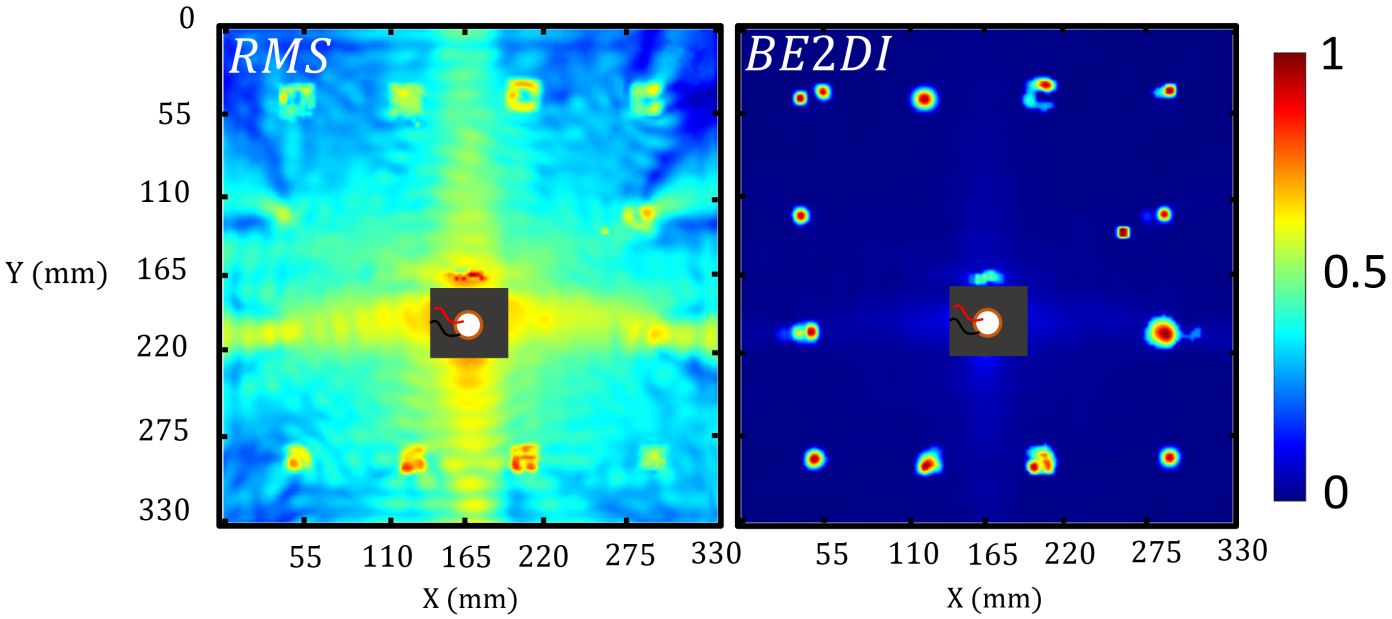

Fig. 9. Normalized results of RMS and BE2DI on $CFRP_2$.

Table.1

The BE2DI performance on $CFRP_2$ in comparison with RMS in terms of CNR.

Inserts	I_1	I_2	I_3	I_4	I_5	I_6	I_7	I_8	I_9	I_{10}	I_{11}	I_{12}
RMS	12.97	4.92	7.34	9.73	1.30	2.58	13.48	8.11	8.34	11.23	-	0.37
BE2DI	**28.23**	**30.68**	**18.12**	**20.05**	**11.76**	**18.10**	**33.24**	**24.80**	**32.35**	**37.85**	**13.91**	**19.88**

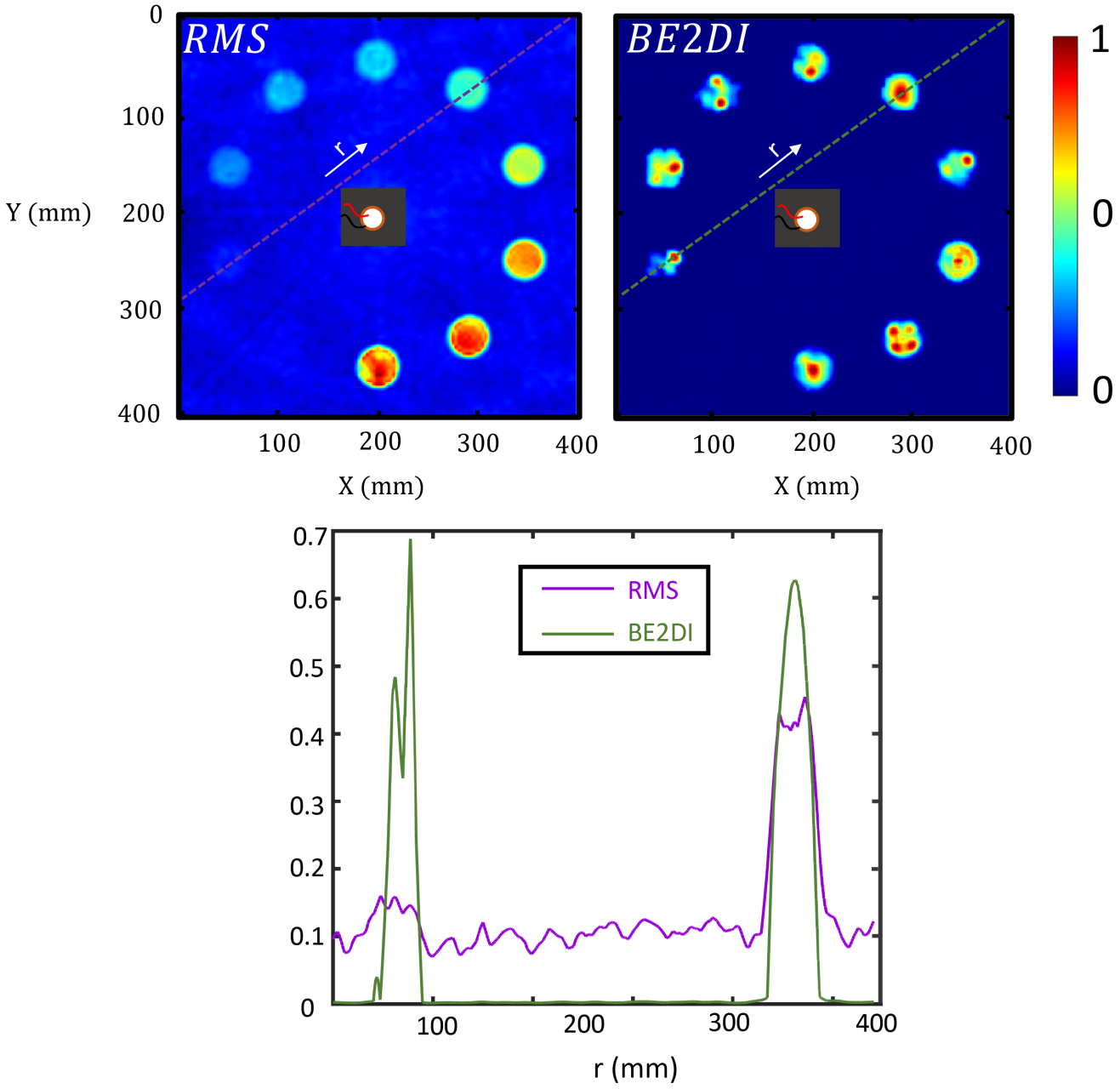

Fig. 10. Normalized results of RMS and BE2DI on AL plate, along with their values along a line passing through FBH_5 and FBH_9.

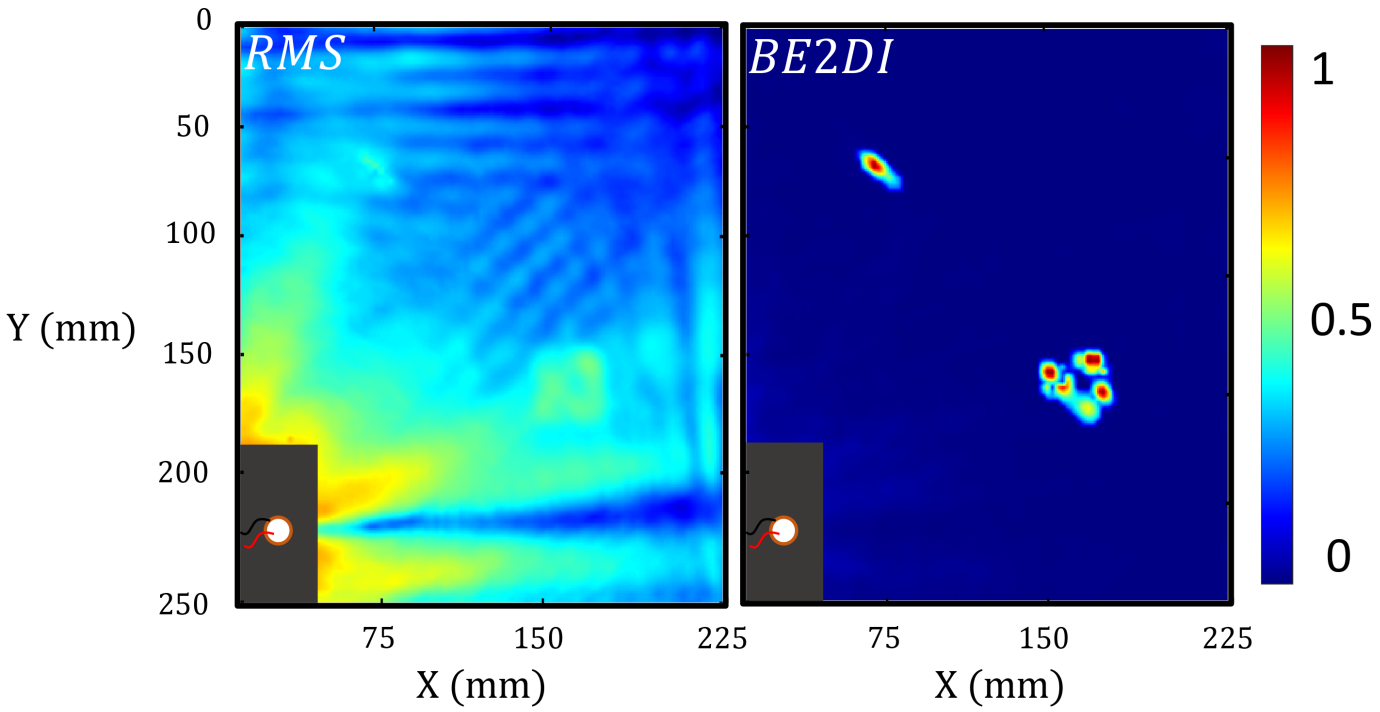

Fig. 11. Normalized results of RMS and BE2DI on CFRP-AR.

Algorithm I: Damage imaging

Input: CDM, $V_z(x, y, f)$, candidate region R;

Initialize: α = 1, w = three times the size of the largest diagonal of R;

1) Compute $entropy = (-\sum_{x=1}^{w} \sum_{y=1}^{w} log\ |IP(x, y, j)|^3)$ inside $w \times w$ windows around the being processed (x_R, y_R) in all ODSs with frequencies $[f_1, f_2, \cdots, f_N]$ and denote it as $\overrightarrow{Ren} = [Ren(f_1), Ren(f_2), \cdots, Ren(f_N)]$ where N represents total number of frequency frame;
2) Sort frequencies by decreasing $\overrightarrow{Ren}$ and list them in $\tilde{f}$;
3) Compute contrast function C per α ranging from 1 to N using (7);
4) Find the first peak of obtained curve in previous step and denote its associated α as α_{ini};
5) Apply Otsu method [45] on $AR\text{-}DI\ (x, y, R, \alpha_{ini})$ and denote the result as $AR\text{-}DI\ _{ini}$;

If # islands in $AR\text{-}DI\ _{ini} > 1$

6) Consider the R as a FP region;

Else

While # islands in $AR\text{-}DI(x, y, R, \alpha) > 1$

7) $\alpha = \alpha - 1$;
8) Compute # islands in the binary image of $AR\text{-}DI\ (x, y, R, \alpha)$ obtained through Otsu method;

End while

End if

9) Consider R as a TP region and compute the associated damage map using (6);

Output: Corresponding damage map $AR\text{-}DI(x, y, R, \alpha)$;

Algorithm II: Masking process

Input: Damage map, candidate region R, CDM, $PCDM$;

1) Select a candidate region R amongst all regions of CDM and denote it as R_s.
2) Compute the following selection index $S_I(R) = \max_{(x_R, y_R) \in R} PCDM(x_R, y_R)$ per R within CDM;
3) Crop out the location of all candidate regions with $S_I > S_I(R_s)$ and no overlap with R_s in the damage map via following two sub steps and denote the result as DM_{masked};
   3.1) Surround a rectangle per candidate;
   3.2) Enlarge constructed rectangles by 5 mm on each side;
4) Apply Otsu [45] on the $PCDM$ and denote the result as $Mask$;
5) Extract the largest region in the $Mask$ and denote it as PZT;
6) Crop out the location of PZT in the DM_{masked} via similar steps as 3.1 and 3.2 and the result is final masked damage map;

Output: Masked damage map;

Highlights

- A Broadband signal is used for excitation and the full wavefield is measured using SLDV.
- A multi-stage vibrometric NDT approach is introduced for defect detection in plates.
- The proposed broadband entropy-based two-stage damage imaging algorithm provides high contrast damage map, revealing both shallow and deep defects.
- The Method is successfully tested on the experimental data of different test specimens containing various defect types.